The cosmic 21-cm revolution: charting the first billion years of our Universe

Andrei Mesinger

July 29, 2019

Contents

Preface

This set of files can be used to create your typescript in LaTeX. You can add packages as necessary.

Remember that references need to be at the chapter level and you may find the package chapterbib useful for this.

About the Author

Remember to include a brief biography of the Authors or Editors, including a photo.

Contributors

Gianni Bernardi
INAF - Istituto di Radio Astronomia
via Gobetti 101, 40129, Bologna, Italy &
Department of Physics and Electronics
Rhodes University
PO Box 94, Grahamstown, 6140, South Africa

Bradley Greig
School of Physics
The University of Melbourne
Parkville, Melboune VIC, Australia

Vibor Jelić
Ruđer Bošković Institute
Zagreb, Croatia

Peter Jones
Department of Physics
University of New England
Acadia, Maine, USA

Jonathan Pritchard
Blackett Laboratory
Imperial College
London, UK

Simon Smith
Department of Electrical Engineering
University of Oxbridge, Camford, USA

Cathryn M. Trott
International Centre for Radio Astronomy Research
Curtin University, Bentley WA, Australia

Chapter 1

Observational strategies: power spectra and images

Gianni Bernardi (INAF-IRA & Rhodes University)

Abstract

This chapter reviews the basics of radio interferometry (van-Citter-Zernike theorem, uv-coverage, image formation calibration) and how they are linked to the measurements of the 21-cm power spectrum and its tomography

1.1 Interferometry overview

The Van Cittert-Zernike theorem expresses the fundamental relationship between the sky spatial brightness (or brightness distribution) I and the quantity measured by an interferometer, i.e. the visibility V (e.g., [**?**]):

$$V_{ij}(\mathbf{b},\lambda) = \int_{\Omega} \bar{I}(\hat{\sigma},\lambda)\, e^{-2\pi i \mathbf{b}\cdot\hat{\sigma}} d\sigma, \tag{1.1}$$

where $\mathbf{b}$ is the baseline vector that separates between antenna i and j and $\hat{sigma}$ is the observing direction (see Figure **??**). The baseline vector is here specified in wevelengths, i.e. $\mathbf{b} = \frac{\mathbf{b}_{\rm m}}{\lambda}$, where $\mathbf{b}_{\rm m}$ is the baseline vector expressed in meters and λ is the observing wavelength. The celestial signal travels an extra path between antenna i and j that correspond to a geometrical time delay $\tau = \mathbf{b}\cdot\hat{\sigma}$, where the world "geometrical" refers to the fact that the delay depends upon the source position in the sky and the relative separation between the two antennas. The sky brightness distribution does not enter directly in equation **??**, but filtered by the antenna primary beam response A that depends upon the direction in the sky and the wavelength, i.e. $\bar{I}(\mathbf{b},\lambda) = A(\mathbf{b},\lambda)I(\mathbf{b},\lambda)$. The response of the primary beam attenuates the sky emission away from the pointing direction, effectively reducing the field of view θ of the instrument. Generally speaking, the size of the field of view is essentially given by the antenna diameter D:

$$\theta \approx \frac{\lambda}{D}. \tag{1.2}$$

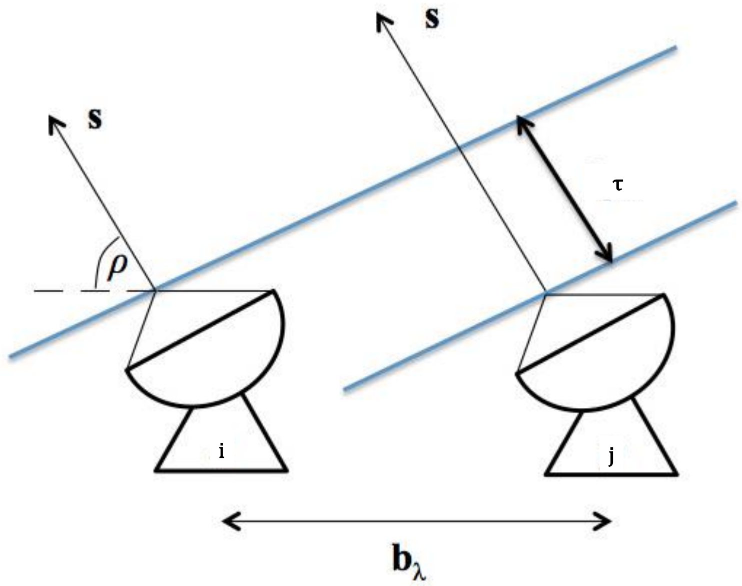

Figure 1.1: A standard schematic of the two element interferometer.

The integral of equation **??** is taken over the source size Ω. Equation **??** is often re-written in a different coordinate system, i.e. the components of the baseline vector (u, v, w) and the reciprocal (l, m, n), where (l, m) are the coordinates in the plane on the sky tangent to the observing direction n (for a detailed discussion on coordinate systems see, for example [**?**]). Using this different coordinate system, equation **??** becomes (e.g., [**?**]):

$$V_{ij}(u, v, w, \lambda) = \int_{\Omega} \bar{I}(l, m, \lambda)\, e^{-2\pi i(ul+vm+wn)} \frac{dl\, dm\, dn}{\sqrt{1-l^2-m^2}}, \tag{1.3}$$

Although low frequency radio observations are intrinsically wide-field, for the purpose of studying the 21 cm observables, we can reduce equation **??** to a two dimensional Fourier transform:

$$V_{ij}(u, v, \lambda) = \int_{\Omega} \bar{I}(l, m, \lambda)\, e^{-2\pi i(ul+vm)} dl\, dm. \tag{1.4}$$

Equation **??** indicates that an *interferometer measures the two dimensional Fourier transform of the spatial sky brightness distribution*. If our goal is to reconstruct the sky brightness distribution, equation **??** can be inverted into its corresponding Fourier pair:

$$\bar{I}(l, m, \lambda) = \int_{-\infty}^{+\infty} V_{ij}(u, v, \lambda)\, e^{2\pi i(ul+vm)} du\, dv. \tag{1.5}$$

Equation **??** is, however, a poor reconstruction of the sky brightness distribution as only one Fourier mode is sampled at the time t. Strictly speaking, indeed, all the quantities in equation **??** and **??** are time variable. In most cases, the time dependence of the primary beam and the sky brightness distribution can be neglected, however, this is not the case for the visibility V as the projection of the baseline vector with respect to the source direction changes significantly throughout a long (e.g. a few hours) track. In this way, many measurements of the visibility coherence function V as $(u,v,)$ change with time can be made, allowing for a better reconstruction of the $\bar{I}(l,m,\lambda)$ function. This methods is commonly described as *filling the uv plane via Earth rotation synthesis* and was invented by [**?**]. The other (complementary) way to fill the *uv* plane is to deploy more antennas on the ground in order to increase the number of instantaneous measurements of independent Fourier modes. If N antennas are connected in an interferometric array, $\frac{N(N-1)}{2}$ instantaneous measurements are made.

The combination of a large number of antennas and the Earth rotation synthesis, defines the sampling function $S(u,v,)$ in the *uv* plane. In any real case, equation **??** can therefore be re-written as:

$$\bar{I}_D(l,m,\lambda) = \int_{-\infty}^{+\infty} S(u,v,)V(u,v,\lambda)\, e^{2\pi i(ul+vm)} du\, dv \tag{1.6}$$

where $\tilde{I}_D$ indicates the sky brightness distribution sampled at a finite number of (u,v) points (often termed *dirty image*) and I dropped the explicit dependence on the antenna pair as redundant at this point. Using the convolution theorem, equation **??** can be re-written as:

$$\bar{I}_D(l,m,\lambda) = \tilde{SV} = \tilde{S} * \tilde{V} = \mathrm{PSF}(l,m,\lambda) * \tilde{V}(l,m,\lambda), \tag{1.7}$$

where the tilde indicates the Fourier transform, $*$ the convolution operation and PSF is the Point Spread Function, i.e. the response of the interferometric array to a point sources which, in our case, is also the Fourier transform of the *uv* coverage.

I will give some examples of sampling functions for different instruments in Section **??**, however, the sampling function always effectively reduces the integral over a finite (often not contiguous) area of the *uv* plane. In particular, the sampled *uv* plane is restricted to a minimum *uv* distance that cannot be shorter than the antenna size and a maximum *uv* distance given by equation **??**. The result of not sampling all the Fourier modes is that the PSF has got "sidelobes", i.e. nulls and secondary lobes that can often contaminate fainter true sky emission. The best reconstruction of the sky brightness distribution $\bar{I}$ requires deconvolution of the dirty image from the PSF.

1.2 21 cm observables: power spectra and images

The ultimate goal of 21 cm observations is to image the spatial distribution of the 21 cm signal as a function of redshift, also known as *21 cm tomography*. Given the curent theoretical predictions, such observations need to achieve mK sensitivity on a few arcminute angular scales (see Chapter 1 in this book). Most of the current arrays, however, only have the sensitivity to perform a statistical detection of the 21 cm, i.e. to measure its power spectrum. Given an intensity field T function of the three dimensional spatial coordinate $\mathbf{x}$, its power spectrum $P(k)$ can be defined as:

$$\langle \tilde{T}^*(\mathbf{k})\tilde{T}(\mathbf{k}')\rangle = (2\pi)^3 P(k)\delta^3(\mathbf{k}-\mathbf{k}') \tag{1.8}$$

where $\langle\rangle$ indicates the ensamble average, $\mathbf{k}$ is the Fourier conjugate of $\mathbf{x}$, tilde the Fourier transform, * the complex conjugate operator and δ the Dirac delta function. In 21 cm observations, power spectra can be computed directly from interferometric image cubes after deconvolution of $\bar{I}_D(l,m,\lambda)$ from the point spread function (e.g., [**?**], [**?**], [**?**], [**?**]). An alternative way to estimate the 21 cm power spectrum that has driven the design and calibration strategies of some of the arrays. Equation **??** already shows that the interferometer is a "natural" spatial power spectrum instrument (e.g., [**?**]). Visibilities can be further Fourier transformed along the frequency axis (the so-called *delay trasform*, [**?**]):

$$\tilde{V}_{ij}(u,v,\tau) = \int_B \bar{I}(l,m,\nu)\, e^{-2\pi i \nu \tau} d\nu \tag{1.9}$$

where B is the observing bandwidth and τ is the geometrical delay. The delay transform is therefore proportional to the three dimensional power spectrum ([**?**]):

$$P(k) \propto \tilde{V}_{ij}(|\mathbf{b}|,\tau), \tag{1.10}$$

where the proportionality constant transforms the visibility units into power units ([**?**]) and the observer units $(\mathbf{b},\tau)$ map directly in k modes parallele and perpendicular to the line of sight (e.g., [**?**]):

$$k_\perp = \frac{2\pi|\mathbf{b}|}{D} = \frac{2\pi\sqrt{u^2+v^2}}{D}, \quad k_\| = \frac{2\pi f_{21} H_0 E(z)}{c\,(1+z)^2}\,\tau, \tag{1.11}$$

where D is the transverse comoving distance, $f_{21} = 1421$ MHz, H_0 is the Hubble constant and $E(z) = \sqrt{\Omega)m(1+z)^3 + \Omega_k(1+z)^2 + \Omega_\Lambda}$. Due to the dependence of the geometrical delay upon frequency, equation **??** is only valid for short baselines, tyipically shorter than a few hundresd meters, for which the geometrical delay is fairly constant across the bandwidht and lines of constant $k_\|$ are practically orthogonal to the $k \perp$ axis ([**?**].

Equation **??** does not only provide a link between visibilities and three dimensional power spectra, but also introduces the concept of "horizon limit" which is the maximum physical delay allowed $\tau_{\max} = \frac{|\mathbf{b}|}{c}$, where c is the speed of light. The most relevant implication of an horizon limit is the definition of a region in power spectrum space where smooth-spectrum foregrounds are confined leaving the remaining area potentially uncontaminated where to measure the 21 cm signal ("EoR window", Figure **??**). Foregrounds can there fore "avoided" with no requirements for subtraction (e.g., [**?**], [**?**], [**?**], [**?**]; see also Chapter **!!!**). The choice of a foreground avoidance strategy versus subtraction plays an important role in planning an experiment, its related observing strategy and the array calibration strategy. **(GB: add a paragraph on imaging!!!**

1.3 Interferometric calibration and 21 cm observations

Celestial signals always experience a corruption due to the non-ideal instrumental response that needs to be corrected for a posteriori, in a process that is known as interferometric calibration. Calibration relies on the definition of a data model where the corruptions are described by antenna based quantities known as Jones matrices. The data model is known as the interferometric measurement equation ([**?**],[**?**]) that will be summarized in the following.

If antenna 1 and antenna 2 measure two orthogonal, linear polarizations x and y, the cross-polarization visibility products can be grouped in a 2×2 matrix $\mathbf{V}$

$$\mathbf{V}_{12}(u,v,\lambda) \equiv \begin{bmatrix} V_{12,xx}(u,v,\lambda) & V_{12,xy}(u,v,\lambda) \\ V_{12,yx}(u,v,\lambda) & V_{12,yy}(u,v,\lambda) \end{bmatrix}. \tag{1.12}$$

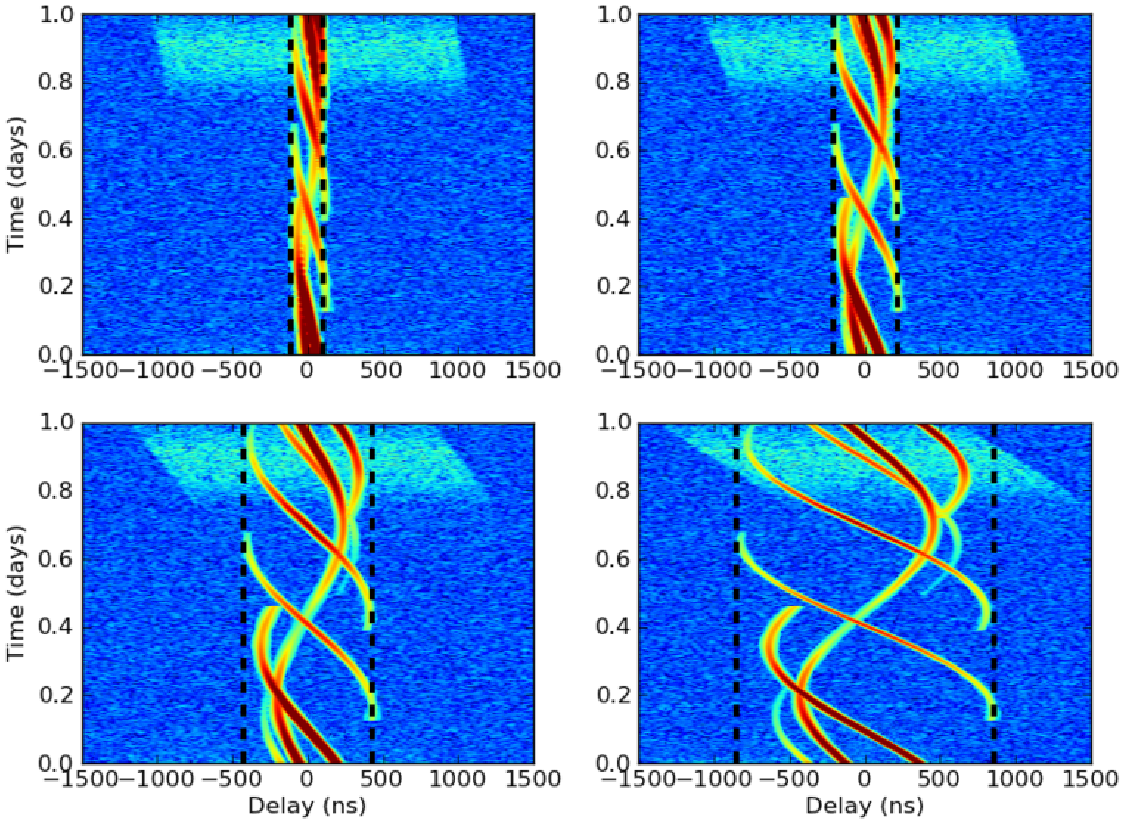

Figure 1.2: Amplitude of delay transformed visibilities as a function of time and delay for a 32 (top let), 64 (top right), 128 (bottom left) and 256 m (bottom right) respectively (from [**?**]). A number of smooth spectrum point sources are simulated as foregrounds and their tracks are clearly bound within the horizon limit (black dashed line). The cyan emission is a fiducial 21 cm model that has power at high delays regardless of the baseline length.

The sky brightness distribution I can also be written as a 2×2 matrix $\mathbf{B}$ using the Stokes parameters as a polarization basis:

$$\mathbf{B}_I(l,m,\lambda) \equiv \begin{bmatrix} I(l,m,\lambda)+Q(l,m,\lambda) & U(l,m,\lambda)+iV(l,m,\lambda) \\ U(l,m,\lambda)-iV(l,m,\lambda) & I(l,m,\lambda)-Q(l,m,\lambda) \end{bmatrix}. \tag{1.13}$$

At this point, equation **??** can be written by including the corruptions represented by the Jones matrices J ([**?**],[**?**]):

$$\mathbf{V}_{12}(u,v,\lambda) = \mathbf{J}_1 \left(\int_\Omega \mathbf{B}_I(l,m,\lambda)\, e^{-2\pi i(ul+vm)} dl\, dm \right) \mathbf{J}_2^H \tag{1.14}$$

Equation **??** is known as the measurement equation and is the core of interferometric calibration. For an array with N antennas, equation **??** can be written for each of the $\frac{N(N-1)}{2}$ visibilities forming an overdetermined system of equations. The development of calibration algorithms is a very active research line ([**?**], [**?**], [**?**], [**?**], [**?**]) although beyond the scope of this chapter and we mention it here for completeness. The solution of the system of calibration equations requires some knowledge of the sky brightness distribution $\mathbf{B}_I$, or a *sky model*. Traditionally this is achieved by observing a calibration source, i.e. a bright, unresolved point source with known spectral and polarization properties. Calibration solutions are then applied to the observed field that, in turn, is then used to improve the sky model $\mathbf{B}_I$ which, in turn, leads to more accurate calibration solutions J in the loop that is traditionally called *self calibration* ([**?**], [**?**]). This approach can lead to a highly accurate calibration (e.g., [**?**], [**?**]).

The advantage of the measurement equation is that it can factorize different physical terms into different matrices. For example, the frequency response of the electronic filters and its time variations essentially affects only the two polarization response and are modeled with a diagonal Jones matrix B:

$$\mathbf{B}(t,\lambda) \equiv \begin{bmatrix} b_x(t,\lambda) & 0 \\ 0 & b_y(t,\lambda) \end{bmatrix}, \tag{1.15}$$

whereas the undesired instrumental leakage between the two orthogonal polarized is represented by a D Jones matrix of the form:

$$\mathbf{D}(t,\lambda) \equiv \begin{bmatrix} 1 & d_x(t,\lambda) \\ -d_y(t,\nu) & 1 \end{bmatrix}, \tag{1.16}$$

and the measurement equation can be written as:

$$\mathbf{V}_{12}(u,v,\lambda) = \mathbf{B}_1\, \mathbf{D}_1 \left(\int_\Omega \mathbf{B}_I(l,m,\lambda)\, e^{-2\pi i(ul+vm)} dl\, dm \right) \mathbf{D}_2^H\, \mathbf{B}_2^H. \tag{1.17}$$

We note that, in principle, the primary beam response should appear as an additional 2×2 Jones matrix before the D matrix. For our pedagogical purposes, we assume that it can be incorporated in the B matrix, although we later illustrate an exception to this assumption.

Retaining only the first order terms, equation **??** can be written as ([**?**]):

$$V_{12,xx}(u,v,\lambda) = b_{1,x} b^*_{2,x}[V_I(u,v,\lambda) - V_Q(u,v,\lambda)] \quad (1.18)$$
$$V_{12,xy}(u,v,\lambda) = b_{1,x} b^*_{2,y}[(d_{1,x} - d^*_{2,y})V_I(u,v,\lambda) + V_U(u,v,\lambda) + iV_V(u,v,\lambda)] \quad (1.19)$$
$$V_{12,yx}(u,v,\lambda) = b_{1,y} b^*_{2,x}[(d_{2,x} - d^*_{1,y})V_I(u,v,\lambda) + V_U(u,v,\lambda) - iV_V(u,v,\lambda)] \quad (1.20)$$
$$V_{12,yy}(u,v,\lambda) = b_{1,y} b^*_{2,y}[V_I(u,v,\lambda) - V_Q(u,v,\lambda)], \quad (1.21)$$

where we dropped the explicit dependence on time and wavelength from the Jones matrices for notation clarity and where $V_{i=I,Q,U,V}$ are the Fourier transforms of the sky brightness matrix B.

This form of the measurement equation offers an intuitive understanding as to why calibration is so important in 21 cm observations. The observed visibilities are essentially a measurement of foreground emission and, in the ideal case, their amplitudes would vary smoothly with frequency, enabling either their avoidance or subtraction. However, the instrumental response inevitably corrupts this smoothness in several ways: because the telescope primary beam is not sufficiently smooth in frequency, because of the filter response or because of reflection along the signal path. Calibration attempts to restore the intrinsic foreground frequency smoothness, however, calibration errors (i.e., deviations from the true B solutions) will corrupt the foreground frequency smoothness. In practice, calibration errors result into foreground power leaking out of the horizon limit and jeopardizing (part of) the EoR window. The corruption of the foreground frequency smoothness will limit the accuracy of any subtraction method (see **Chapter !!!**). *The effectiveness of foreground separation, proven in ideal cases, depends significantly on the accuracy of interferometric calibration.*

There are a few topics of active research in improving the accuracy of interferometric calibration:

- *sky models*. Ideally, the sky brightness model matrix B_I (equation **??** and **??**) should include the whole sky emission. This is pratically impossible as part of the sky signal is the unknown that we want to discover (the 21 cm signal) and part of the signal has not been observed before or, even if observed, its detailed properties are not know sufficiently well.

  Efforts to achieve the most accurate calibration include in the brightness matrix B_I thousands of compact sources in an aread larger than the telescope field of view (e.g., [**?**]. This sky model may still be insufficient as it does not include sources over the whole sky nor Galactic diffuse emission. Galactic emission contributes to most of the power on angular scales $\theta > 10 - 20$ arcmin ([**?**], [**?**]), therefore a compact sources sky model is not adequate for baselines shorter than a few tens of meters. Excluding short baselines from the calibration solutions would prevent the problem but can bias the solution ([**?**]) if the system of calibration equation is not regularized appropriately ([**?**]).

  Another form of sky model incompleteness is related to angular resolution: due its finite resolution, sources that are not completely unresolved are nevertheless treated as point-like and this too biases the calibration solutions, leading to an excess of foreground contamination in the EoR window ([**?**]).

[?], [?] and [?] show that effect of sky model incompleteness on calibration eventually leads to artifacts in the form of ghost-like sources in interferometric images, most of the times fainter than the image noise level. They also show that the ghost pattern is stronger for regularly spaced arrays and if the sky model is more incomplete. [?] formalize the effect of incomplete sky models on calibration as a leakage of foreground power in the EoR window.

Significant effort is currently ongoing in order to improve the all-sky compact-source model via wider and deeper low frequency surveys (e.g., [?], [?], [?]), more accurate low frequency catalogues ([?]) and even improvements of the Galactic diffuse emission observations ([?], [?]). Some of the calibration strategies described in the next sections may, however, mitigate the requirements of extremely accurate sky models;

- *instrument/primary beam models*. A complete knowledge of a sky model may not be, by itself, sufficient for an accurate calibration of 21 cm observations as the brightness matrix B_I appears in the calibration equation multiplied by the antenna primary beam (equation **??** and **??**) and the measurement of an intrinsic sky model requires the separation from the primary beam effect.

  Unlike steerable dishes, most 21 cm interferometers are constituted of dipoles fixed on the ground, in some cases clustered together to form tiles or stations that can digitally pointed in a sky direction via a physical delay (e.g., like the MWA and LOFAR arrays, see Section **??**). As station beams are formed to track the source on the sky, the station projected area changes with time and the shape of the primay beam changes significantly (Figure **??**). This effect leads to time variable sky models with variations that are larger away from the pointing direction due to the large variations in the sidelobe pattern. For examples, sky sources that are well within the main lobe of the primary beam in Figure **??** will experience relatively negligible variations throughout an observation, the opposite will occur to sources located well outside the main lobe as the enter and exit different sidelobes.

  Primary beams are also frequency variable and, at first order, their size scales with wavelength (similar to the angular resolution, equation **??**), i.e. rather smoothly. However, in the sidelobe region, such variation becomes rather abrupt as the sidelobe pattern changes too, therefore the source can be at the peak of a sidelobe at a certain frequency and in the sidelobe null at another frequency. As a final remark, stations are not perfectly equal to each other, due to manifacturing reasons or mutual coupling between their elements (e.g., [?], [?]), therefore the sky brightness matrix B_I is potentially different for each baseline as the primary beams are different. The left panel of Figure **??** attempt to quantify this effect in a simulated case: variations in the sidelobe region can be as large as $\sim 30\%$.

  If not accurately modeled and taken into account, the aforementioned effects can bias the calibration solution and, again, corrupt the foreground smoothness. [?], [?] and [?] have developed methods to incorporate time and frequency variable primary beams in interferometric images, however, the accuracy of the correction is limited by the accurace of the primary beam model. Increasing effort is therefore being placed in accurante modeling and measuring primary beams (e.g., [?], [?], [?], [?]);

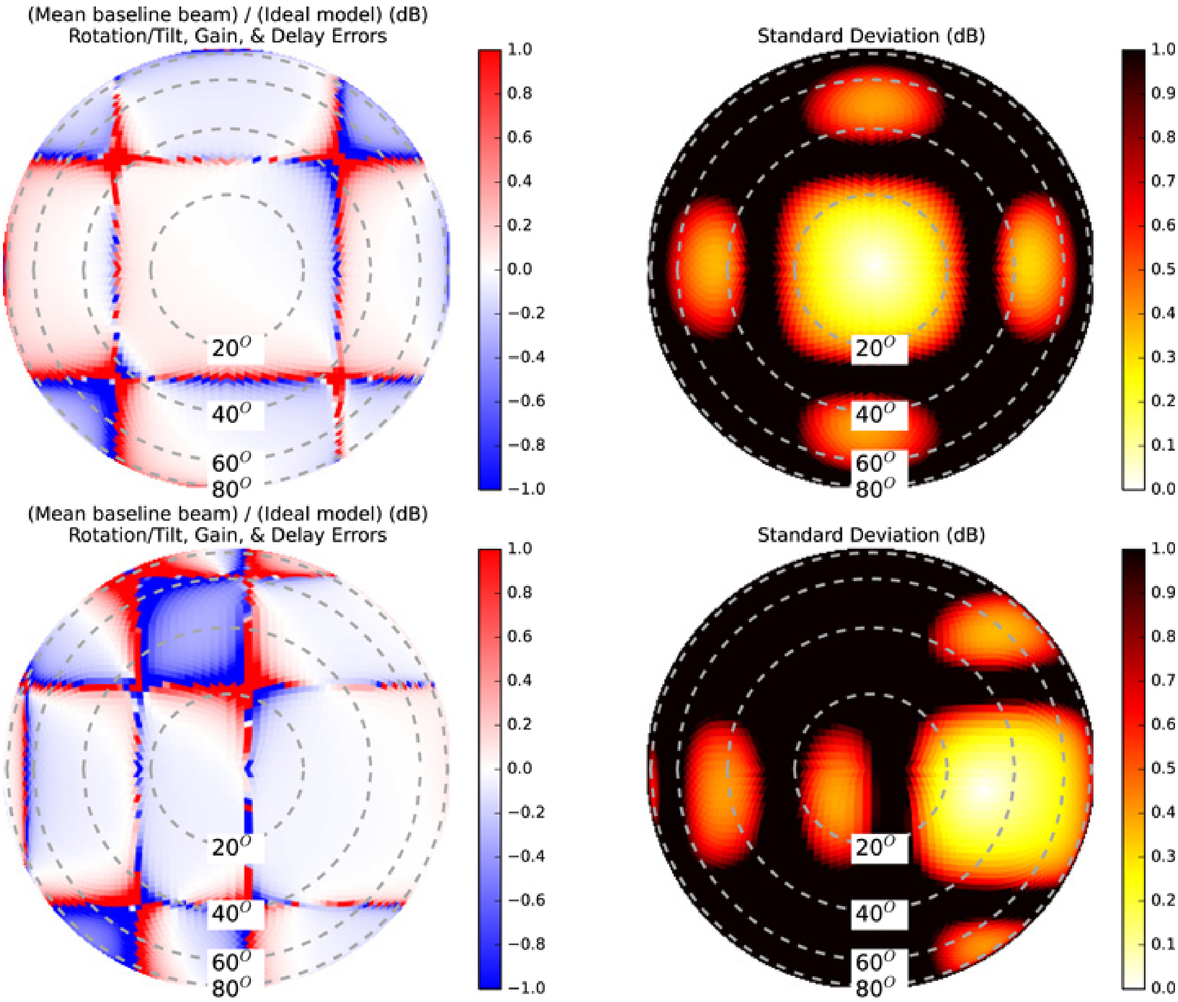

Figure 1.3: Example of primary beam variations as the MWA station points at zenith (top right) and $\sim 30^{\circ}$ away from zenith (bottom right) at 150 MHz. The left column shows the fractional variation of individual station beam models, with respect to the nominal primary beam (right column, from [**?**]. It is visibile how different sidelob pattern is when pointing towards two different directions. It should also be noticed that the magnitude of the first lobe is at the $\sim 10\%$ level and the large null areas around the lobes. The specific pattern is due to the regular shape of the MWA station, where 16 dipoles are arrange in a square 4×4 grid.

- *polarization leakage calibration*. Equation **??** and **??** show that, even if the 21 cm signal is unpolarized, care needs to be taken against the contamination from polarized foreground emission. Most point sources are unpolarized below 200 MHz ([**?**], [**?**], [**?**]), therefore the assumption of an unpolarized sky model is well justified. However, errors in the matrix B different between the xx and yy polarizations would lead to polarized emission to leak into total intensity, particularly on short baselines, where polarized foreground emission is brighter ([**?**], [**?**], [**?**], [**?**]). Polarized foregrounds Faraday rotated by the intersetllar medium that leak to total intensity may be a severe contamination of the 21 cm signal (e.g., [**?**], [**?**], [**?**]).

  Even if calibration errors are negligible, low frequency antennas have a non negligible polarized response across their wide field of view. If we call the Jones matrix that represents the polarized primary beam response $E \equiv E(l,m,\lambda)$, its associate measurement equation can be written as ([**?**]):

$$\begin{aligned}
\begin{bmatrix} V_{12,I}(u,v,\lambda) \\ V_{12,Q}(u,v,\lambda) \\ V_{12,U}(u,v,\lambda) \\ V_{12,V}(u,v,\lambda) \end{bmatrix} &= \int_\Omega \mathbf{S}^{-1}[\mathbf{E}_1 \otimes \mathbf{E}_2^H]\mathbf{S} \begin{bmatrix} I(l,m,\lambda) \\ Q(l,m,\lambda) \\ U(l,m,\lambda) \\ V(l,m,\lambda) \end{bmatrix} e^{-2\pi i(ul+vm)} dl\, dm = \\
&= \int_\Omega \mathbf{A}(l,m,\lambda) \begin{bmatrix} I(l,m,\lambda) \\ Q(l,m,\lambda) \\ U(l,m,\lambda) \\ V(l,m,\lambda) \end{bmatrix} e^{-2\pi i(ul+vm)} dl\, dm, \qquad (1.22)
\end{aligned}$$

  where $\mathbf{S}$ is the matrix that relates the intrisic Stokes parameters to the observer $-y$ frame, $\otimes$ is the outer product. The visibilities are written as a four-element vector as this form shows that the outer product of the beam Jones matrices maps the intrinsic Stoke parameters into the observed ones:

$$\begin{pmatrix} I' \leftarrow I & I' \leftarrow Q & I' \leftarrow U & I' \leftarrow V \\ Q' \leftarrow I & Q' \leftarrow Q & Q' \leftarrow U & Q' \leftarrow V \\ U' \leftarrow I & U' \leftarrow Q & U' \leftarrow U & U' \leftarrow V \\ V' \leftarrow I & V' \leftarrow Q & V' \leftarrow U & V' \leftarrow V \end{pmatrix}. \qquad (1.23)$$

  The first raw of the matrix shows how the four intrisinc Stokes parameters contribute to the observed total intensity and, therefore, how polarized foregrounds leak into the 21 cm signal even in absence of any calibration errors: any polarized signal (Stokes Q and U) will contaminate the observed total intensity signal, and the magnitude of the contamination increases away from the ponting direction. An example of $\mathbf{A}$ matrix is shonw in Figure **??**.

  Calibration of the polarization leakage remains a challenging task. It can be mitigated by extending the sky model to include polarization (e.g. [**?**]), although modeling the diffuse Galactic foreground - the brightest component - is not straightforward and requires accurate imaging. [**?**] showed that also polarized foregrounds may be avoided if they are not highly Faraday rotated by the interestellar medium, although a more extensive characterization of polarized foreground properties is needed.

- *ionospheric distortions*

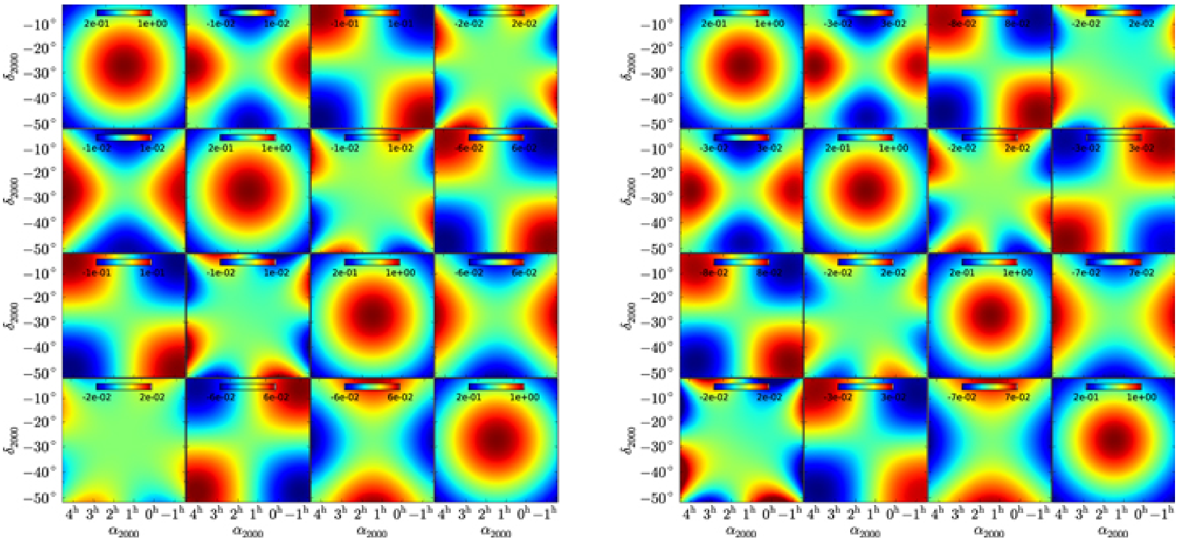

Figure 1.4: Examples of **A** matrices at 130 (left) and 150 MHz respectively (from [**?**]). The matrix maps the intrinsic Stokes parameters into observed ones: the diagonal terms represent the expected primary beam shapes, whereas the off-diagonal terms represents leakage terms. The second, the third and the fourth element of the first row show how Stokes parameters Q, U and V respectively contaminate the total intensity signal.

1.3.1 Direction dependent calibration

In the previous section I have summarized the calibration equations and the main effects that lead to calibration errors that, in turn, may jeopardize foreground separation. The calibration formalism describe

1.3.2 Redundant calibration

An interferometric array where most of the baselines have the same length and orientation is called *redundant* as they measure the same Fourier mode of the sky brightness distribution. Redundant array configurations are often not appealing as they have poor imaging performances as they do not measure sufficient Fourier modes to reconstruct accurate sky images. However, a maximally redundant array where the antennas are laid out in a regularly spaced square grid offers the maximum power spectrum sensitivity on the $k_\perp$ modes corresponding to the most numerous baselines. This criterium has inspired the highly redundant layouts of the MIT Epoch of Reionization experiment ([**?**]), the Precision Array to Probe the Epoch of Reionization (PAPER, [**?**]) and partly driven the updated MWA.

One of the advantages of a redundant array is that it enables a different calibration strategy called *redundant calibration*. In redundant calibration the form of the measurement equation does not change and can be written, for a single polarization, like equation **??**:

$$V_{12,xx}(u,v,\lambda) = b_{1,x} b^*_{2,x} y_{12,xx}(u,v,\lambda), \tag{1.24}$$

with the difference now that the model visibility y is not tied to a sky model, but it is solved for, simply assuming that it is the same for each group of redundant baselines [**?**], [**?**]). In

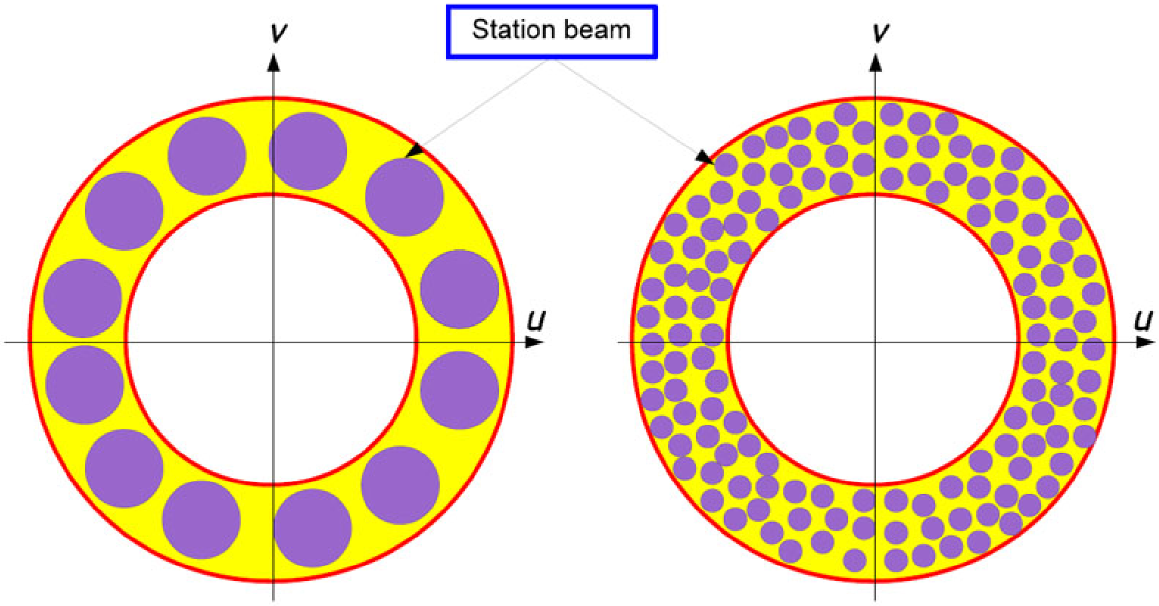

Figure 1.5: uv footprint.

other words, redundant calibration is independent on the sky model and, therefore, bypasses entirely the biases related to sky model incompleteness described in Section **??**. However, as redundant calibration is not tied to any physical (i.e. sky-based) spatial or spectral model, its solutions have degeneracies that need to be solved for by using a sky model (e.g., [**?**], [**?**]). In particular, spectral calibration, which is critical for foreground separation, cannot currently be obtained using redundant calibration and requires a sky-based calibration. [**?**] suggest that sky model incompleteness can bias this calibration step, in a way similar to what happens with a traditional calibration scheme.

Redundant calibration is also prone to effects that break the assumption of redundancy, the most common being errors in the antenna positions and different primary beams for different antennas. Even if antenna position errors can be reduced to have a negligible impact on redundant calibration [**?**], the effect of primary beam variations amongts the different antennas on redundant calibration is still largely unknown.

1.4 Array design and observing strategies

I will conclude this chapter by discussing how the various interferometric effects discuss so far impact the choice of array designs and the consequent observing strategies. Beyond the obvious sensitivity requirement, decisions need to be taken as to which layout to adopt, which antenna size and these choice are intrinsically related to calibration and foreground separation strategies. For instance a filled *uv*-coverage (between the minimum and the maximum station separation) is highly desirable for imaging, modeling and subtracting foregrounds. It is not a stringent requirement for power spectrum measurement and in the avoidance strategy. The choice of station size determines the minimum k

*valueaccessibleandthefootprintofeach*uv*measurement.Indeedeachvisibilityisnotasinglepointinthe*uvp

As examples, I will use four existing low frequency arrays that, concidentally, span the range of parameters of interest:

- effect of the field of view, calibratability, uv cell, drift scan versus tracking, suppression of sources outside the main lobe ionosphere
- uv coverage choices power spectra vs images, redundant vs pseud random (reconstructing sky brightness), minimum/maximum k mode accessible... avoidance (compact) vs subtraction (less compact)
- obviously sensitivity
- *Low Frequency Array (LOFAR)*. LOFAR is an array mainly located in The Nerthelands but it include also remote stations acroos Europe. Each station
- Murchison Widefield Array (MWA)
- Precision Array to Probe the Epoch of Reionization (PAPER)
- Hydrogen Epoch of Reionization Array (HERA)
- Square Kilomtre Array (SKA)

Bibliography

[1] N. Barry, B. Hazelton, I. Sullivan, M. F. Morales, and J. C. Pober. Calibration requirements for detecting the 21 cm epoch of reionization power spectrum and implications for the SKA. *MNRAS*, 461:3135–3144, September 2016.

[2] A. P. Beardsley, B. J. Hazelton, I. S. Sullivan, P. Carroll, N. Barry, M. Rahimi, B. Pindor, C. M. Trott, J. Line, D. C. Jacobs, M. F. Morales, J. C. Pober, G. Bernardi, J. D. Bowman, M. P. Busch, F. Briggs, R. J. Cappallo, B. E. Corey, A. de Oliveira-Costa, J. S. Dillon, D. Emrich, A. Ewall-Wice, L. Feng, B. M. Gaensler, R. Goeke, L. J. Greenhill, J. N. Hewitt, N. Hurley-Walker, M. Johnston-Hollitt, D. L. Kaplan, J. C. Kasper, H. S. Kim, E. Kratzenberg, E. Lenc, A. Loeb, C. J. Lonsdale, M. J. Lynch, B. McKinley, S. R. McWhirter, D. A. Mitchell, E. Morgan, A. R. Neben, N. Thyagarajan, D. Oberoi, A. R. Offringa, S. M. Ord, S. Paul, T. Prabu, P. Procopio, J. Riding, A. E. E. Rogers, A. Roshi, N. Udaya Shankar, S. K. Sethi, K. S. Srivani, R. Subrahmanyan, M. Tegmark, S. J. Tingay, M. Waterson, R. B. Wayth, R. L. Webster, A. R. Whitney, A. Williams, C. L. Williams, C. Wu, and J. S. B. Wyithe. First Season MWA EoR Power spectrum Results at Redshift 7. *ApJ*, 833:102, December 2016.

[3] G. Bernardi, A. G. de Bruyn, M. A. Brentjens, B. Ciardi, G. Harker, V. Jelić, L. V. E. Koopmans, P. Labropoulos, A. Offringa, V. N. Pandey, J. Schaye, R. M. Thomas, S. Yatawatta, and S. Zaroubi. Foregrounds for observations of the cosmological 21 cm line. I. First Westerbork measurements of Galactic emission at 150 MHz in a low latitude field. *A&A*, 500:965–979, June 2009.

[4] G. Bernardi, A. G. de Bruyn, G. Harker, M. A. Brentjens, B. Ciardi, V. Jelić, L. V. E. Koopmans, P. Labropoulos, A. Offringa, V. N. Pandey, J. Schaye, R. M. Thomas, S. Yatawatta, and S. Zaroubi. Foregrounds for observations of the cosmological 21 cm line. II. Westerbork observations of the fields around 3C 196 and the North Celestial Pole. *A&A*, 522:A67, November 2010.

[5] R. Byrne, M. F. Morales, B. Hazelton, W. Li, N. Barry, A. P. Beardsley, R. Joseph, J. Pober, I. Sullivan, and C. Trott. Fundamental Limitations on the Calibration of Redundant 21 cm Cosmology Instruments and Implications for HERA and the SKA. *ApJ*, 875:70, April 2019.

[6] P. A. Carroll, J. Line, M. F. Morales, N. Barry, A. P. Beardsley, B. J. Hazelton, D. C. Jacobs, J. C. Pober, I. S. Sullivan, R. L. Webster, G. Bernardi, J. D. Bowman, F. Briggs,

R. J. Cappallo, B. E. Corey, A. de Oliveira-Costa, J. S. Dillon, D. Emrich, A. Ewall-Wice, L. Feng, B. M. Gaensler, R. Goeke, L. J. Greenhill, J. N. Hewitt, N. Hurley-Walker, M. Johnston-Hollitt, D. L. Kaplan, J. C. Kasper, H. Kim, E. Kratzenberg, E. Lenc, A. Loeb, C. J. Lonsdale, M. J. Lynch, B. McKinley, S. R. McWhirter, D. A. Mitchell, E. Morgan, A. R. Neben, D. Oberoi, A. R. Offringa, S. M. Ord, S. Paul, B. Pindor, T. Prabu, P. Procopio, J. Riding, A. E. E. Rogers, A. Roshi, N. U. Shankar, S. K. Sethi, K. S. Srivani, R. Subrahmanyan, M. Tegmark, N. Thyagarajan, S. J. Tingay, C. M. Trott, M. Waterson, R. B. Wayth, A. R. Whitney, A. Williams, C. L. Williams, C. Wu, and J. S. B. Wyithe. A high reliability survey of discrete Epoch of Reionization foreground sources in the MWA EoR0 field. *MNRAS*, 461:4151–4175, October 2016.

[7] S. Choudhuri, S. Bharadwaj, S. S. Ali, N. Roy, H. T. Intema, and A. Ghosh. The angular power spectrum measurement of the Galactic synchrotron emission in two fields of the TGSS survey. *MNRAS*, 470:L11–L15, September 2017.

[8] T. J. Cornwell and P. N. Wilkinson. A new method for making maps with unstable radio interferometers. *MNRAS*, 196:1067–1086, September 1981.

[9] E. de Lera Acedo, P. Bolli, F. Paonessa, G. Virone, E. Colin-Beltran, N. Razavi-Ghods, I. Aicardi, A. Lingua, P. Maschio, J. Monari, G. Naldi, M. Piras, and G. Pupillo. SKA aperture array verification system: electromagnetic modeling and beam pattern measurements using a micro UAV. *Experimental Astronomy*, 45:1–20, March 2018.

[10] E. de Lera Acedo, C. M. Trott, R. B. Wayth, N. Fagnoni, G. Bernardi, B. Wakley, L. V. E. Koopmans, A. J. Faulkner, and J. G. bij de Vaate. Spectral performance of SKA Log-periodic Antennas I: mitigating spectral artefacts in SKA1-LOW 21 cm cosmology experiments. *MNRAS*, 469:2662–2671, August 2017.

[11] J. Dowell, G. B. Taylor, F. K. Schinzel, N. E. Kassim, and K. Stovall. The LWA1 Low Frequency Sky Survey. *MNRAS*, 469:4537–4550, August 2017.

[12] T. L. Grobler, C. D. Nunhokee, O. M. Smirnov, A. J. van Zyl, and A. G. de Bruyn. Calibration artefacts in radio interferometry - I. Ghost sources in Westerbork Synthesis Radio Telescope data. *MNRAS*, 439:4030–4047, April 2014.

[13] T. L. Grobler, A. J. Stewart, S. J. Wijnholds, J. S. Kenyon, and O. M. Smirnov. Calibration artefacts in radio interferometry - III. Phase-only calibration and primary beam correction. *MNRAS*, 461:2975–2992, September 2016.

[14] J. P. Hamaker, J. D. Bregman, and R. J. Sault. Understanding radio polarimetry. I. Mathematical foundations. *A&AS*, 117:137–147, May 1996.

[15] G. Harker, S. Zaroubi, G. Bernardi, M. A. Brentjens, A. G. de Bruyn, B. Ciardi, V. Jelić, L. V. E. Koopmans, P. Labropoulos, G. Mellema, A. Offringa, V. N. Pandey, A. H. Pawlik, J. Schaye, R. M. Thomas, and S. Yatawatta. Power spectrum extraction for redshifted 21-cm Epoch of Reionization experiments: the LOFAR case. *MNRAS*, 405:2492–2504, July 2010.

[16] N. Hurley-Walker, J. R. Callingham, P. J. Hancock, T. M. O. Franzen, L. Hindson, A. D. Kapińska, J. Morgan, A. R. Offringa, R. B. Wayth, C. Wu, Q. Zheng, T. Murphy, M. E. Bell, K. S. Dwarakanath, B. For, B. M. Gaensler, M. Johnston-Hollitt, E. Lenc, P. Procopio, L. Staveley-Smith, R. Ekers, J. D. Bowman, F. Briggs, R. J. Cappallo, A. A. Deshpande, L. Greenhill, B. J. Hazelton, D. L. Kaplan, C. J. Lonsdale, S. R. McWhirter, D. A. Mitchell, M. F. Morales, E. Morgan, D. Oberoi, S. M. Ord, T. Prabu, N. U. Shankar, K. S. Srivani, R. Subrahmanyan, S. J. Tingay, R. L. Webster, A. Williams, and C. L. Williams. GaLactic and Extragalactic All-sky Murchison Widefield Array (GLEAM) survey - I. A low-frequency extragalactic catalogue. *MNRAS*, 464:1146–1167, January 2017.

[17] H. T. Intema, P. Jagannathan, K. P. Mooley, and D. A. Frail. The GMRT 150 MHz all-sky radio survey. First alternative data release TGSS ADR1. *A&A*, 598:A78, February 2017.

[18] D. C. Jacobs, J. Burba, J. D. Bowman, A. R. Neben, B. Stinnett, L. Turner, K. Johnson, M. Busch, J. Allison, M. Leatham, V. Serrano Rodriguez, M. Denney, and D. Nelson. First Demonstration of ECHO: an External Calibrator for Hydrogen Observatories. *PASP*, 129(3):035002, March 2017.

[19] S. Kazemi, S. Yatawatta, S. Zaroubi, P. Lampropoulos, A. G. de Bruyn, L. V. E. Koopmans, and J. Noordam. Radio interferometric calibration using the SAGE algorithm. *MNRAS*, 414:1656–1666, June 2011.

[20] A. Liu, M. Tegmark, S. Morrison, A. Lutomirski, and M. Zaldarriaga. Precision calibration of radio interferometers using redundant baselines. *MNRAS*, 408:1029–1050, October 2010.

[21] D. A. Mitchell, L. J. Greenhill, R. B. Wayth, R. J. Sault, C. J. Lonsdale, R. J. Cappallo, M. F. Morales, and S. M. Ord. Real-Time Calibration of the Murchison Widefield Array. *IEEE Journal of Selected Topics in Signal Processing*, 2:707–717, November 2008.

[22] M. F. Morales, B. Hazelton, I. Sullivan, and A. Beardsley. Four Fundamental Foreground Power Spectrum Shapes for 21 cm Cosmology Observations. *ApJ*, 752:137, June 2012.

[23] M. F. Morales and J. Hewitt. Toward Epoch of Reionization Measurements with Wide-Field Radio Observations. *ApJ*, 615:7–18, November 2004.

[24] A. Mouri Sardarabadi and L. V. E. Koopmans. Quantifying suppression of the cosmological 21-cm signal due to direction-dependent gain calibration in radio interferometers. *MNRAS*, 483:5480–5490, March 2019.

[25] A. R. Neben, J. N. Hewitt, R. F. Bradley, J. S. Dillon, G. Bernardi, J. D. Bowman, F. Briggs, R. J. Cappallo, B. E. Corey, A. A. Deshpande, R. Goeke, L. J. Greenhill, B. J. Hazelton, M. Johnston-Hollitt, D. L. Kaplan, C. J. Lonsdale, S. R. McWhirter, D. A. Mitchell, M. F. Morales, E. Morgan, D. Oberoi, S. M. Ord, T. Prabu, N. Udaya Shankar,

K. S. Srivani, R. Subrahmanyan, S. J. Tingay, R. B. Wayth, R. L. Webster, A. Williams, and C. L. Williams. Beam-forming Errors in Murchison Widefield Array Phased Array Antennas and their Effects on Epoch of Reionization Science. *ApJ*, 820:44, March 2016.

[26] C. D. Nunhokee, G. Bernardi, S. A. Kohn, J. E. Aguirre, N. Thyagarajan, J. S. Dillon, G. Foster, T. L. Grobler, J. Z. E. Martinot, and A. R. Parsons. Constraining Polarized Foregrounds for EoR Experiments. II. Polarization Leakage Simulations in the Avoidance Scheme. *ApJ*, 848:47, October 2017.

[27] A. Parsons, J. Pober, M. McQuinn, D. Jacobs, and J. Aguirre. A Sensitivity and Array-configuration Study for Measuring the Power Spectrum of 21 cm Emission from Reionization. *ApJ*, 753:81, July 2012.

[28] A. R. Parsons, J. C. Pober, J. E. Aguirre, C. L. Carilli, D. C. Jacobs, and D. F. Moore. A Per-baseline, Delay-spectrum Technique for Accessing the 21 cm Cosmic Reionization Signature. *ApJ*, 756:165, September 2012.

[29] A. H. Patil, S. Yatawatta, L. V. E. Koopmans, A. G. de Bruyn, M. A. Brentjens, S. Zaroubi, K. M. B. Asad, M. Hatef, V. Jelić, M. Mevius, A. R. Offringa, V. N. Pandey, H. Vedantham, F. B. Abdalla, W. N. Brouw, E. Chapman, B. Ciardi, B. K. Gehlot, A. Ghosh, G. Harker, I. T. Iliev, K. Kakiichi, S. Majumdar, G. Mellema, M. B. Silva, J. Schaye, D. Vrbanec, and S. J. Wijnholds. Upper Limits on the 21 cm Epoch of Reionization Power Spectrum from One Night with LOFAR. *ApJ*, 838:65, March 2017.

[30] A. H. Patil, S. Yatawatta, S. Zaroubi, L. V. E. Koopmans, A. G. de Bruyn, V. Jelić, B. Ciardi, I. T. Iliev, M. Mevius, V. N. Pandey, and B. K. Gehlot. Systematic biases in low-frequency radio interferometric data due to calibration: the LOFAR-EoR case. *MNRAS*, 463:4317–4330, December 2016.

[31] T. J. Pearson and A. C. S. Readhead. Image Formation by Self-Calibration in Radio Astronomy. *ARAA*, 22:97–130, 1984.

[32] U.-L. Pen, T.-C. Chang, C. M. Hirata, J. B. Peterson, J. Roy, Y. Gupta, J. Odegova, and K. Sigurdson. The GMRT EoR experiment: limits on polarized sky brightness at 150 MHz. *MNRAS*, 399:181–194, October 2009.

[33] J. C. Pober, A. R. Parsons, J. E. Aguirre, Z. Ali, R. F. Bradley, C. L. Carilli, D. DeBoer, M. Dexter, N. E. Gugliucci, D. C. Jacobs, P. J. Klima, D. MacMahon, J. Manley, D. F. Moore, I. I. Stefan, and W. P. Walbrugh. Opening the 21 cm Epoch of Reionization Window: Measurements of Foreground Isolation with PAPER. *ApJ*, 768:L36, May 2013.

[34] P. Procopio, R. B. Wayth, J. Line, C. M. Trott, H. T. Intema, D. A. Mitchell, B. Pindor, J. Riding, S. J. Tingay, M. E. Bell, J. R. Callingham, K. S. Dwarakanath, B.-Q. For, B. M. Gaensler, P. J. Hancock, L. Hindson, N. Hurley-Walker, M. Johnston-Hollitt, A. D. Kapińska, E. Lenc, B. McKinley, J. Morgan, A. Offringa, L. Staveley-Smith,

C. Wu, and Q. Zheng. A High-Resolution Foreground Model for the MWA EoR1 Field: Model and Implications for EoR Power Spectrum Analysis. *PASA*, 34:e033, August 2017.

[35] G. Pupillo, G. Naldi, G. Bianchi, A. Mattana, J. Monari, F. Perini, M. Poloni, M. Schiaffino, P. Bolli, A. Lingua, I. Aicardi, H. Bendea, P. Maschio, M. Piras, G. Virone, F. Paonessa, Z. Farooqui, A. Tibaldi, G. Addamo, O. A. Peverini, R. Tascone, and S. J. Wijnholds. Medicina array demonstrator: calibration and radiation pattern characterization using a UAV-mounted radio-frequency source. *Experimental Astronomy*, 39:405–421, June 2015.

[36] M. Ryle and A. Hewish. The synthesis of large radio telescopes. *MNRAS*, 120:220, 1960.

[37] R. J. Sault, J. P. Hamaker, and J. D. Bregman. Understanding radio polarimetry. II. Instrumental calibration of an interferometer array. *A&AS*, 117:149–159, May 1996.

[38] T. W. Shimwell, C. Tasse, M. J. Hardcastle, A. P. Mechev, W. L. Williams, P. N. Best, H. J. A. Röttgering, J. R. Callingham, T. J. Dijkema, F. de Gasperin, D. N. Hoang, B. Hugo, M. Mirmont, J. B. R. Oonk, I. Prandoni, D. Rafferty, J. Sabater, O. Smirnov, R. J. van Weeren, G. J. White, M. Atemkeng, L. Bester, E. Bonnassieux, M. Brüggen, G. Brunetti, K. T. Chyży, R. Cochrane, J. E. Conway, J. H. Croston, A. Danezi, K. Duncan, M. Haverkorn, G. H. Heald, M. Iacobelli, H. T. Intema, N. Jackson, M. Jamrozy, M. J. Jarvis, R. Lakhoo, M. Mevius, G. K. Miley, L. Morabito, R. Morganti, D. Nisbet, E. Orrú, S. Perkins, R. F. Pizzo, C. Schrijvers, D. J. B. Smith, R. Vermeulen, M. W. Wise, L. Alegre, D. J. Bacon, I. M. van Bemmel, R. J. Beswick, A. Bonafede, A. Botteon, S. Bourke, M. Brienza, G. Calistro Rivera, R. Cassano, A. O. Clarke, C. J. Conselice, R. J. Dettmar, A. Drabent, C. Dumba, K. L. Emig, T. A. Enßlin, C. Ferrari, M. A. Garrett, R. T. Génova-Santos, A. Goyal, G. Gürkan, C. Hale, J. J. Harwood, V. Heesen, M. Hoeft, C. Horellou, C. Jackson, G. Kokotanekov, R. Kondapally, M. Kunert-Bajraszewska, V. Mahatma, E. K. Mahony, S. Mandal, J. P. McKean, A. Merloni, B. Mingo, A. Miskolczi, S. Mooney, B. Nikiel-Wroczyński, S. P. O'Sullivan, J. Quinn, W. Reich, C. Roskowiński, A. Rowlinson, F. Savini, A. Saxena, D. J. Schwarz, A. Shulevski, S. S. Sridhar, H. R. Stacey, S. Urquhart, M. H. D. van der Wiel, E. Varenius, B. Webster, and A. Wilber. The LOFAR Two-metre Sky Survey. II. First data release. *A&A*, 622:A1, February 2019.

[39] O. M. Smirnov. Revisiting the radio interferometer measurement equation. I. A full-sky Jones formalism. *A&A*, 527:A106, March 2011.

[40] O. M. Smirnov. Revisiting the radio interferometer measurement equation. II. Calibration and direction-dependent effects. *A&A*, 527:A107, March 2011.

[41] O. M. Smirnov and C. Tasse. Radio interferometric gain calibration as a complex optimization problem. *MNRAS*, 449:2668–2684, May 2015.

[42] C. Tasse. Nonlinear Kalman filters for calibration in radio interferometry. *A&A*, 566:A127, June 2014.

[43] A. Richard Thompson, James M. Moran, and Jr. Swenson, George W. *Interferometry and Synthesis in Radio Astronomy, 3rd Edition*. 2017.

[44] N. Thyagarajan, N. Udaya Shankar, R. Subrahmanyan, W. Arcus, G. Bernardi, J. D. Bowman, F. Briggs, J. D. Bunton, R. J. Cappallo, B. E. Corey, L. deSouza, D. Emrich, B. M. Gaensler, R. F. Goeke, L. J. Greenhill, B. J. Hazelton, D. Herne, J. N. Hewitt, M. Johnston-Hollitt, D. L. Kaplan, J. C. Kasper, B. B. Kincaid, R. Koenig, E. Kratzenberg, C. J. Lonsdale, M. J. Lynch, S. R. McWhirter, D. A. Mitchell, M. F. Morales, E. H. Morgan, D. Oberoi, S. M. Ord, J. Pathikulangara, R. A. Remillard, A. E. E. Rogers, D. Anish Roshi, J. E. Salah, R. J. Sault, K. S. Srivani, J. B. Stevens, P. Thiagaraj, S. J. Tingay, R. B. Wayth, M. Waterson, R. L. Webster, A. R. Whitney, A. J. Williams, C. L. Williams, and J. S. B. Wyithe. A Study of Fundamental Limitations to Statistical Detection of Redshifted H I from the Epoch of Reionization. *ApJ*, 776:6, October 2013.

[45] H. Vedantham, N. Udaya Shankar, and R. Subrahmanyan. Imaging the Epoch of Reionization: Limitations from Foreground Confusion and Imaging Algorithms. *ApJ*, 745:176, February 2012.

[46] M. White, J. E. Carlstrom, M. Dragovan, and W. L. Holzapfel. Interferometric Observation of Cosmic Microwave Background Anisotropies. *ApJ*, 514:12–24, March 1999.

[47] M. H. Wieringa. An investigation of the telescope based calibration methods 'redundancy' and 'self-cal'. *Experimental Astronomy*, 2:203–225, 1992.

[48] S. J. Wijnholds, T. L. Grobler, and O. M. Smirnov. Calibration artefacts in radio interferometry - II. Ghost patterns for irregular arrays. *MNRAS*, 457:2331–2354, April 2016.

[49] S. Yatawatta. Distributed radio interferometric calibration. *MNRAS*, 449:4506–4514, June 2015.

[50] S. Yatawatta, A. G. de Bruyn, M. A. Brentjens, P. Labropoulos, V. N. Pandey, S. Kazemi, S. Zaroubi, L. V. E. Koopmans, A. R. Offringa, V. Jelić, O. Martinez Rubi, V. Veligatla, S. J. Wijnholds, W. N. Brouw, G. Bernardi, B. Ciardi, S. Daiboo, G. Harker, G. Mellema, J. Schaye, R. Thomas, H. Vedantham, E. Chapman, F. B. Abdalla, A. Alexov, J. Anderson, I. M. Avruch, F. Batejat, M. E. Bell, M. R. Bell, M. Bentum, P. Best, A. Bonafede, J. Bregman, F. Breitling, R. H. van de Brink, J. W. Broderick, M. Brüggen, J. Conway, F. de Gasperin, E. de Geus, S. Duscha, H. Falcke, R. A. Fallows, C. Ferrari, W. Frieswijk, M. A. Garrett, J. M. Griessmeier, A. W. Gunst, T. E. Hassall, J. W. T. Hessels, M. Hoeft, M. Iacobelli, E. Juette, A. Karastergiou, V. I. Kondratiev, M. Kramer, M. Kuniyoshi, G. Kuper, J. van Leeuwen, P. Maat, G. Mann, J. P. McKean, M. Mevius, J. D. Mol, H. Munk, R. Nijboer, J. E. Noordam, M. J. Norden, E. Orru, H. Paas, M. Pandey-Pommier, R. Pizzo, A. G. Polatidis, W. Reich, H. J. A. Röttgering, J. Sluman, O. Smirnov, B. Stappers, M. Steinmetz, M. Tagger, Y. Tang, C. Tasse, S. ter Veen, R. Vermeulen, R. J. van Weeren, M. Wise, O. Wucknitz, and P. Zarka. Initial deep LOFAR observations of epoch of reionization windows. I. The north celestial pole. *A&A*, 550:A136, February 2013.

[51] H. Zheng, M. Tegmark, V. Buza, J. S. Dillon, H. Gharibyan, J. Hickish, E. Kunz, A. Liu, J. Losh, A. Lutomirski, S. Morrison, S. Narayanan, A. Perko, D. Rosner, N. Sanchez, K. Schutz, S. M. Tribiano, M. Valdez, H. Yang, K. Z. Adami, I. Zelko, K. Zheng, R. P. Armstrong, R. F. Bradley, M. R. Dexter, A. Ewall-Wice, A. Magro, M. Matejek, E. Morgan, A. R. Neben, Q. Pan, R. F. Penna, C. M. Peterson, M. Su, J. Villasenor, C. L. Williams, and Y. Zhu. MITEoR: a scalable interferometer for precision 21 cm cosmology. *MNRAS*, 445:1084–1103, December 2014.

[52] H. Zheng, M. Tegmark, J. S. Dillon, A. Liu, A. R. Neben, S. M. Tribiano, R. F. Bradley, V. Buza, A. Ewall-Wice, H. Gharibyan, J. Hickish, E. Kunz, J. Losh, A. Lutomirski, E. Morgan, S. Narayanan, A. Perko, D. Rosner, N. Sanchez, K. Schutz, M. Valdez, J. Villasenor, H. Yang, K. Zarb Adami, I. Zelko, and K. Zheng. Brute-force mapmaking with compact interferometers: a MITEoR northern sky map from 128 to 175 MHz. *MNRAS*, 465:2901–2915, March 2017.

Chapter 2

Future prospects

Author Name

Abstract

This chapter discusses some important things

2.1 Forthcoming interferometric ground based instruments and upgrades

2.1.1 The Hydrogen Epoch of Reionization Array

The Hydrogen Epoch of Reionization Array (HERA) is an array currently under construction in the Karoo reserve area in South Africa - following the conclusion of the PAPER experiment. HERA is built following the approach used for PAPER: a highly redundant array to maximize the sensitivity on a number of power spectrum modes measured using the avoidance approach. In order to increase the sensitivity with respect to PAPER, it employs 14 m diameter dishes that, in the final configuration, will be densely packed in a highly redundant hexagonal array configuration of $\sim$ 350 m diameter. HERA is built with the purpose to provide a complete statistical characterization of cosmic reionization: its high brightness sensitivity configuration leads to a significant ($>$ 10) power spectrum detection in the $0.2 < k < 0.4$ Mpc-1 range throughout reionization (i.e., 6 ¡ z ¡ 12; Pober et al., 2014; deBoer et al., 2017), fully constraining the evolution of the IGM neutral Hydrogen fraction. As the avoidance approach does not take advantage of foreground modeling, particular attention was paid to prevent the instrumental frequency response from corrupting intrinsically smooth foregrounds (Ewall-Wice et al., 2015; Patra et al., 2017). HERA is currently under construction, with more than 200 dishes deployed and science observations routinely carried out (Carilli et al. 2018, Kohn et al. 2019). New feeds that extend the sensitivity to the 50-250 MHz (i.e. enabling observations of the Cosmic Dawn) are currently deployed for testing. In summary, HERA is planned to deliver a complete characterization of cosmic reionization and to attempt the detection of the Cosmic Dawn. Given its redundant configuration, imaging capabilities remain limited and will be the target of a next generation experiment.

2.1.2 The Large aperture Experiment to detect the Dark Ages

The Large aperture Experiment to detect the Dark Ages (LEDA) is located in Owens Valley, California. It operates in the 30-88 MHz frequency range corresponding to $15 < z < 46$, therefore seeking to detect the 21 cm signal from the Cosmic Dawn. It is equipped to attempt the measurement of both the global signal via individual dipoles equipped with custom-built calibration sources and 21 cm fluctuations via an array of 256 dipoles. Dipoles are pseudo randomly distributed to achieve an essentially filled array within a 200 m diameter core, providing excellent imaging capabilities to Galactic diffuse emission - the brightest foreground component. The LEDA approach to measure the 21 cm signal can be versatile, allowing to image and subtract foregrounds but also to isolate them in the power spectrum domain without any specific modeling. Current simulations shows that if IGM heating occurs efficiently at z 16, LEDA would be able to detect the 21 cm power spectrum at $k \sim 0.1$ Mpc-1 with a 10 signal to noise ratio in 3000 hours. First observations have set a 108 (mK)2 upper limits on the 21 cm power spectrum at k = 0.1 Mpc-1 at z = 18.4 (Eastwood et al. 2019)

2.2 A Section

Lorem ipsum dolor sit amet, consectetur adipiscing elit. Duis eu egestas erat. Maecenas tincidunt lacinia tincidunt. Mauris id lectus nec neque feugiat condimentum vitae at diam. In vel orci nunc, non commodo mauris. Vivamus ipsum enim, vulputate quis pharetra non, molestie quis felis. Vivamus porttitor placerat turpis at accumsan. Nunc tortor velit, faucibus a rhoncus nec, blandit non elit. Nam consectetur lectus eu nisi blandit dapibus rhoncus dui tempus. Mauris fermentum dolor vel ipsum vulputate sit amet ultricies tortor lacinia. Donec ut nibh erat. Morbi nec mi ante. Integer nec vestibulum diam. Donec tincidunt pellentesque quam, ut interdum mauris venenatis condimentum. Nam condimentum, augue in aliquet gravida, neque dui elementum eros, id semper eros purus sed felis. Curabitur in justo sit amet sapien ultrices hendrerit at quis nibh. Quisque iaculis pulvinar tincidunt.

$$\begin{aligned} C(12) &= \left[\vec{\pi} \cdot \vec{\phi}(x+r)\right] \\ &\approx 1 - \text{const}\frac{r^2}{L^2}\int_r^L \frac{x\mathrm{d}x}{x^2} + \cdots \\ &\approx 1 - \text{const}\frac{r^2}{L^2}\ln\frac{x\mathrm{d}x}{x^2} + \cdots . \end{aligned} \tag{2.1}$$

Aenean tellus risus, porta sit amet porta vitae, tincidunt ut felis. Class aptent taciti sociosqu ad litora torquent per conubia nostra, per inceptos himenaeos. Vestibulum ante ipsum primis in faucibus orci luctus et ultrices posuere cubilia Curae; Phasellus pulvinar placerat velit auctor egestas. Vivamus euismod fringilla tincidunt. Sed ut magna felis, id sollicitudin nunc. Quisque a dui eu erat consectetur egestas a quis justo. Aenean euismod congue diam, vel posuere urna fermentum sit amet. Lorem ipsum dolor sit amet, consectetur adipiscing elit. Mauris faucibus lacus eget est mollis auctor. Donec at nibh ligula, et posuere massa. Phasellus quis leo diam [**?**]. Donec aliquam blandit risus, eu venenatis ante euismod eu. Curabitur cursus justo id arcu condimentum feugiat. Integer sapien urna, vulputate et adipiscing nec, convallis et justo. Suspendisse in ipsum at felis ornare interdum [**?**],

Figure 2.1: This is figure 1 in chapter 1.

Table 2.1: Greek Letters.

α	β	γ	δ	ϵ	ε	ζ	η
θ	ϑ	γ	κ	λ	μ	ν	ξ
o	π	ϖ	ρ	ϱ	σ	ς	
τ	υ	ϕ	φ	χ	ψ	ω	
Γ	Δ	Θ	Λ	Ξ	Π	Σ	Υ
Φ	Ψ	Ω					

Cras adipiscing sagittis nunc vel luctus. Suspendisse volutpat augue quis erat semper consequat dignissim tellus euismod. Morbi hendrerit, tellus id aliquam iaculis, nibh leo tincidunt eros, vitae varius ligula felis in mi.

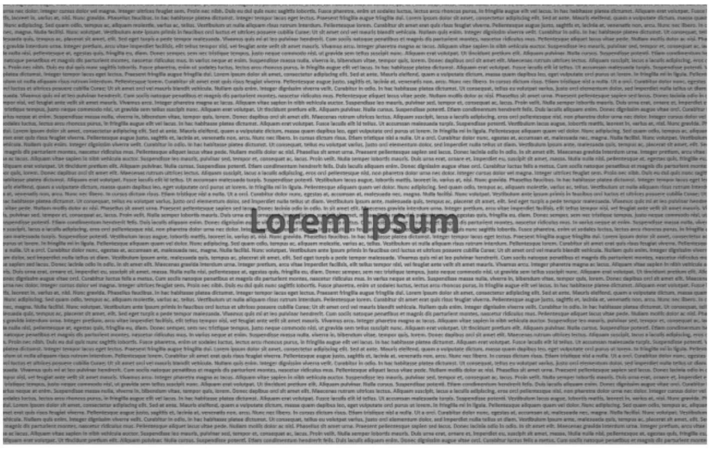

Figure 2.2: This is figure 2 in chapter 1.

Bibliography

[1] KI Diamantaras and SY Kung. *Principal component neural networks: theory and applications*. John Wiley & Sons, Inc. New York, NY, USA, 1996.

[2] D. Tulone and S. Madden. PAQ: Time Series Forecasting for Approximate Query Answering in Sensor Networks. In *Proceedings of the 3rd European Workshop on Wireless Sensor Networks*, pages 21–37. Springer, 2006.